ADVANCED MATERIALS TECHNOLOGIES
www.advmattechnol.de

Flexible Multilayer Metasurfaces: Design and Applications on Foldable and Conformable Substrates

*Yilin Shi, Hao Dai, Renjie Tang, Jianghong Wu, Yingchun Wu, Jieren Song, Yalan Si, Hongtao Lin, and Lan Li**

Metasurfaces offer effective optical modulation and compact solutions for integrated optoelectronic circuits. Multilayer metasurfaces surpass single-layer counterparts in functionalities, enabling more complex manipulation of phase, amplitude, and polarization. However, existing multilayer metasurfaces lack reconfigurability based on flexible configurations, limiting their applications in dynamic and shape-constrained scenarios. Here, a multilayer metasurface platform utilizing a foldable and conformable flexible structure is introduced. The foldability enables coupled or decoupled multilayer metasurfaces by reconfigurable folding alignment. To validate this technology, the previously established flexible metasurface fabrication techniques are employed. The coupled multilayer metasurface is demonstrated by an inverse-designed 1D multilayer zoom metalens that achieves a numerical aperture (NA) from 0.80 to 0.12 by altering the polarization state of incident light from X- to Y-polarization. For the decoupled multilayer metasurface, a refractive-meta hybrid system is demonstrated, featuring metalens that operates on curved surfaces and can switch between a near-diffraction-limited telephoto mode and an 80° wide-angle mode. The exceptional performance of the two validated devices on this platform highlights its superiority as a comprehensive design platform for multilayer metasurfaces. Notably, its potential for operation on non-planar forms offers promising applications for miniaturized optoelectronic devices such as augmented reality displays and wearable medical devices.

1. Introduction

With the miniaturization of integrated optoelectronic devices for important applications such as augmented reality (AR) displays[1] and wearable medical devices,[2] there is an increasing demand for multifunctional and flexible optical components that are adaptable to shape constraints. However, traditional optical components based on geometrical optics struggle to decouple shape from optical function, leading to an inherent conflict with these requirements. Metasurfaces[3] consisting of subwavelength-scale dimensions structures, so-called meta-atoms, offer unprecedented control over light scattering, including phase, amplitude, and polarization, thus inspiring the development of next-generation advanced compact devices such as beam deflectors,[4] structured light projectors,[5] holograms,[6] and metalenses.[7] To expand the optical functionalities, researchers have proposed multilayer structures[7h,8] to increase design flexibility by allowing adjustments to the materials and spacings of different layers. Nowadays, multilayer metasurfaces[9] primarily focus on two structure designs: coupled multilayer devices[8d–f,i] and decoupled multilayer devices,[7h,8a–c,g,h,j] distinguished by whether coupling occurs between the metasurface layers-coupling arises when the interlayer distance is less than a wavelength, and is absent when the distance is significantly greater. Coupled multilayer structures provide new design freedom by allowing interactions between

Y. Shi
Zhejiang University
Hangzhou 310027, China
Y. Shi, R. Tang, J. Wu, Y. Wu, L. Li
Zhejiang Key Laboratory of 3D Micro/Nano Fabrication and Characterization
School of Engineering
Westlake University
Hangzhou 310030, China
E-mail: lilan@westlake.edu.cn

The ORCID identification number(s) for the author(s) of this article can be found under https://doi.org/10.1002/admt.202402130

DOI: 10.1002/admt.202402130

Y. Shi, R. Tang, J. Wu, Y. Wu, L. Li
Institute of Advanced Technology
Westlake Institute for Advanced Study
Hangzhou 310024, China
H. Dai, J. Song, Y. Si, H. Lin
Key Laboratory of Micro-Nano Electronics and Smart System of Zhejiang Province
College of Information Science and Electronic Engineering
Zhejiang University
Hangzhou 310027, China
L. Li
Westlake Institute for Optoelectronics
Fuyang, Hangzhou, Zhejiang 311421, China

meta-atoms due to their coupling characteristics. However, this interaction limits reconfigurability, as it is highly sensitive to variations in external conditions such as refractive index, meta-atom spacing, and incident angle. Conversely, decoupled multilayer structures, which lack this coupling, enable functional reconfiguration by adjusting the horizontal or axial distances between layers. Researchers have used these two types of designs to achieve great functionalities in metasurfaces, such as achromatic,[8a,f] angular aberration correction,[8d] zoom imaging,[7h,8j,10] quantitative phase imaging,[8c] beam steering,[8g] and difference imaging,[8b] showcasing the vast potential of multilayer metasurfaces, especially for metalens. However, existing multilayer metasurface technologies face challenges in supporting both types of flexible multilayer structures, thereby restricting their potential for broader applications.

Current strategies in the fabrication of multilayer metasurfaces include 3D printing,[8e] multilayer lithography,[11] and mechanical assembly.[7h,8a–c,g,h,j] 3D printing can enable the fabrication of multilayer metasurfaces in the microwave band.[8e] However, it becomes challenging at shorter wavelengths due to the limited precision of 3D printing.[8e] Multilayer lithography[11] enables precise nanofabrication and alignment at visible wavelengths, facilitating the development of decoupled multilayer metasurfaces with wide field of view (FOV) imaging capabilities.[11] However, the obtained multilayer structures are fixed after fabrication, significantly limiting the reconfigurability of decoupled metasurfaces. Another commonly used method is mechanical assembly, which involves assembling pre-fabricated metasurface devices.[7h,8a–c,g,h,j] This technique allows for versatile control over the spacing between devices, possessing the potential for constructing both types of multilayer metasurface structures. The decoupled type, which enables zoom imaging[7h,8j] and beam steering[8g] based on this approach, has been reported by adjusting the vertical[7h,8j] and lateral[8g] distances between layers. Nevertheless, the existing structures utilizing this method rely on rigid substrates,[7h,8a–c,g,h,j] limiting their value in emerging applications such as AR displays and wearable medical devices. In contrast, flexible metasurfaces, with their conformable,[12] stretchable,[7c] and bendable[13] characteristics, exhibit remarkable reconfigurability and the capability to operate on non-planar substrates. However, reports on their foldability and adaptability for multilayer designs are still lacking.

In this study, we present a novel multilayer metasurface platform that facilitates the development of reconfigurable and conformable multilayer metasurface devices while supporting the design of coupled and decoupled configurations based on flexible metasurface. First, we developed a 1D zoom metalens using an adjoint-based topology optimization algorithm for coupled multilayer metasurfaces formed by inward folding. By changing the polarization of incident light from X to Y, this metalens can achieve significant zoom capabilities, with a numerical aperture (NA) ranging from 0.80 to 0.12. Second, we combined scalar simulations and vector simulations to jointly design a metalens that works on curved substrates as a refractive-meta hybrid system. The system can switch between wide-angle (80° FOV) and near-diffraction-limited telephoto modes. This work drives innovation in advanced imaging systems, adaptive optics, and reconfigurable optics, highlighting the practical benefits of this scheme and establishing a solid foundation for future research.

2. Principles and Methods

We construct our design based on our previous research on the stretchable properties of flexible metasurfaces,[7c] which can be further extended to a multilayered metasurface platform. **Figure 1** illustrates the conceptual framework of our entire work. Specifically, we utilize flexible substrates, Polydimethylsiloxane (PDMS), and a GeO_2-based transfer method to create a vertically asymmetric flexible metasurface structure, enabling reconfigurable folding alignment for multilayer metasurfaces. By aligning the layers inward or outward, we can effectively control the interlayer distance to be less than or greater than a wavelength, thereby facilitating the coupling or decoupling of the electromagnetic field distribution between meta-atoms, as shown in Figure S1 (Supporting Information). When coupling occurs, the original electromagnetic field distribution of the meta-atoms is disrupted, making the phase modulation mechanism more complex and the output phase non-pre-compiled. In contrast, during decoupling, the electromagnetic field distribution of the meta-atoms remains relatively independent, allowing the output phase to be pre-compiled.[8d] These coupling and decoupling effects enable the creation of functional devices, as shown in Figure 1a,b. Notably, this reconfigurable alignment also allows multiple devices to be combined for functional reconfiguration. Additionally, due to the adhesive properties of the substrate, the packaging cost for the multilayer structure is effectively reduced. Furthermore, because of the substrate's conformability, our devices can operate on non-planar surfaces, as illustrated in Figure 1b.

2.1. Polarization-Multiplexed 1D Metalens Based on Coupled Multilayer Structure

We first realized a coupled multilayer metasurface by inward folding operation (Figure 3a), which works as a 1D polarization-multiplexed multilayer zoom metalens. Each meta-atom structure consists of amorphous silicon (a-Si) with a period (P), a height (h), and a width (W), which is partially encapsulated by PDMS and tightly integrated between the upper and lower layers. The multilayer configuration offers greater design flexibility compared to single-layer structures.[8d] At the same time, polarization control enables efficient adjustment of the NA without relying on external media[7a,14] or intricate mechanical structures.[7h,8j,10] By varying the polarization of the incident light from X to Y, the NA of the zoom metalens changes from 0.80 to 0.12.

Specifically, our design used an adjoint-based topology optimization algorithm,[15] which is primarily categorized into density[16] and boundary optimization.[17] Density optimization iteratively transforms the dielectric constant distribution between structural and environmental media into a meaningful binary pattern. However, treating every element as an optimization target can result in an irregular distribution, which increases processing complexity. Conversely, boundary optimization refines only the structure's boundaries, such as the length and width of a rectangle, starting from an existing binary structure. The resulting design is more accessible to the process.

Here, we use a boundary optimization algorithm to solve this problem, and the algorithm's framework is illustrated in **Figure 2**. The FOM can be formulated as follows:

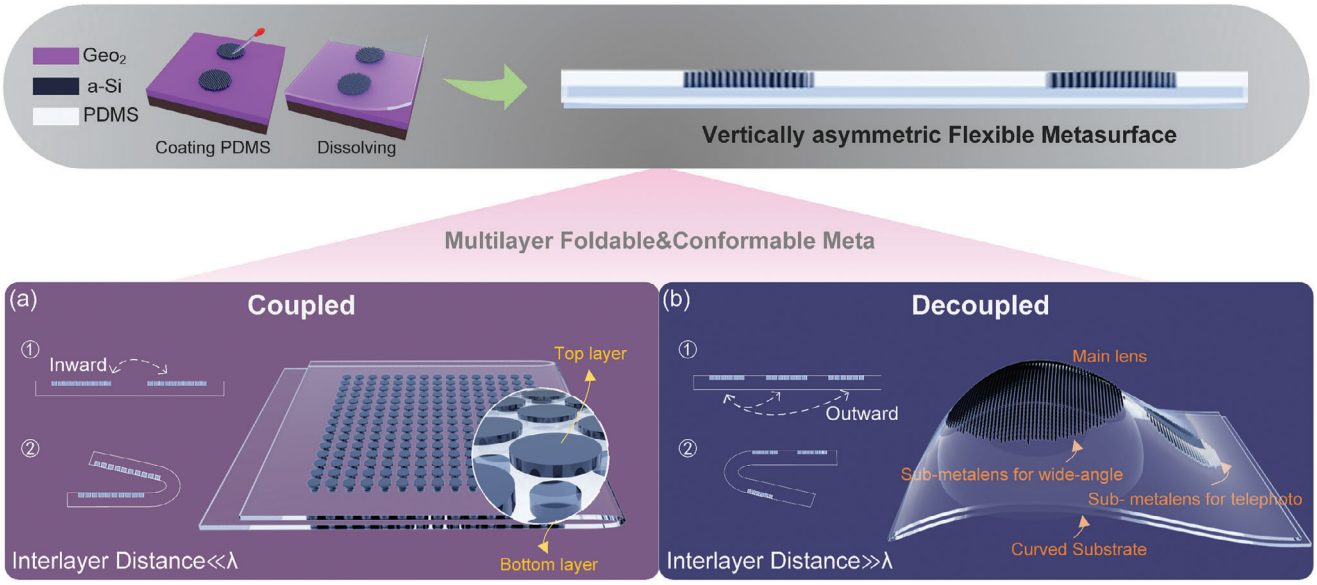

Figure 1. A multilayer metasurface platform based on foldable and conformable substrate: a) Coupled multilayer device. b) Decoupled multilayer device.

$$\mathrm{FOM} = \int \left| \vec{E}(r) \cdot \vec{E}_{ideal}(r) \right| dr \tag{1}$$

where $\int dr$ is defined as the spatial integration over a reference plane one wavelength away from the metalens. r denotes a spatial point. $\vec{E}(r)$ and $\vec{E}_{ideal}(r)$ represent the simulated and ideal electromagnetic field distribution of the metalens with a given NA, respectively. Equation (1) illustrates the correlation between $\vec{E}(r)$ and $\vec{E}_{ideal}(r)$, a larger FOM indicates that $\vec{E}(r)$ has a phase distribution more consistent with $\vec{E}_{ideal}(r)$, along with a higher amplitude. The specific expression for $\vec{E}_{ideal}$ is as follows:

$$\vec{E}_{ideal}(r) = e^{i*\Phi(r)}, \Phi(r) = \Phi_0 - \frac{2\pi}{\lambda}\left(\sqrt{f^2 + (r - r_0)^2} - f\right) \tag{2}$$

where $\Phi(r)$ represents the desired phase profile, Φ_0 indicates the initial phase, r_0 denotes the center of the metalens. f indicates the desired focal length of the metalens with a given NA.

The essence of adjoint optimization is to compute the gradient of the objective function with respect to the optimized structure, expressed as $\frac{\partial FOM}{\partial W}$ here. This is accomplished by executing forward and adjoint simulations in each iteration. In the forward simulation, plane waves with X- and Y-polarizations are used separately as incident sources from the flexible substrate to calculate the forward electric field distribution, $\vec{E}^{forward}$. In the backward simulation, the derivatives $\frac{\partial FOM}{\partial \vec{E}(r)}$ corresponding to X- and Y-polarized states are used separately as adjoint sources to calculate the adjoint electric field distribution, $\vec{E}^{adjoint}$. After completing both forward and adjoint simulations, $\frac{\partial FOM}{\partial W}$ can be expressed according to the boundary conditions of Maxwell's equations as follows:[15]

$$\frac{\partial FOM}{\partial W} = jw \int_X \left[\left(\varepsilon_{\mathrm{a-Si}} - \varepsilon_{PDMS}\right) \vec{E}_{||}^{forward} \vec{E}_{||}^{adjoint} + \left(\frac{1}{\varepsilon_{\mathrm{a-Si}}} - \frac{1}{\varepsilon_{PDMS}}\right) \vec{D}_{\perp}^{forward} \vec{D}_{\perp}^{adjoint} \right] dx \tag{3}$$

where w is the angular frequency, X is the side edge of the meta-atom, x is a point on the side edge of the meta-atom, ε_{PDMS} is the dielectric constant of the PDMS surrounding the nanopillars, and $\varepsilon_{\mathrm{a-Si}}$ is the dielectric constant of the a-Si meta-atom. $\vec{E}_{||}^{forward}$ and $\vec{E}_{||}^{adjoint}$ represent the tangential components of the electric field in the forward and adjoint fields, respectively. $\vec{D}_{\perp}^{forward}$ and $\vec{D}_{\perp}^{adjoint}$ represent the normal components of the electric displacement vector in the forward and adjoint fields, respectively. The sum of the gradients at each point along the edge surface of the meta-atom, $\frac{\partial FOM}{\partial W}$, is then used as a deformation in the normal direction to ensure that the meta-atom remains easily machinable as a rectangle.

We compare the *FOM* for each polarization state denoted as FOM_{X-pol} and FOM_{Y-pol} at the end of each iteration to determine the final gradient G for the subsequent optimization, as shown in the following Equation (4):

$$G = \frac{1}{\left(FOM_{X-pol}/FOM_{Y-pol}\right)} * \frac{\partial FOM_{X-pol}}{\partial W} + \frac{1}{\left(FOM_{Y-pol}/FOM_{X-pol}\right)} * \frac{\partial FOM_{Y-pol}}{\partial W} \tag{4}$$

The gradient obtained from Equation (4) ensures excellent and consistent performance for both X- and Y-polarized light. Then,

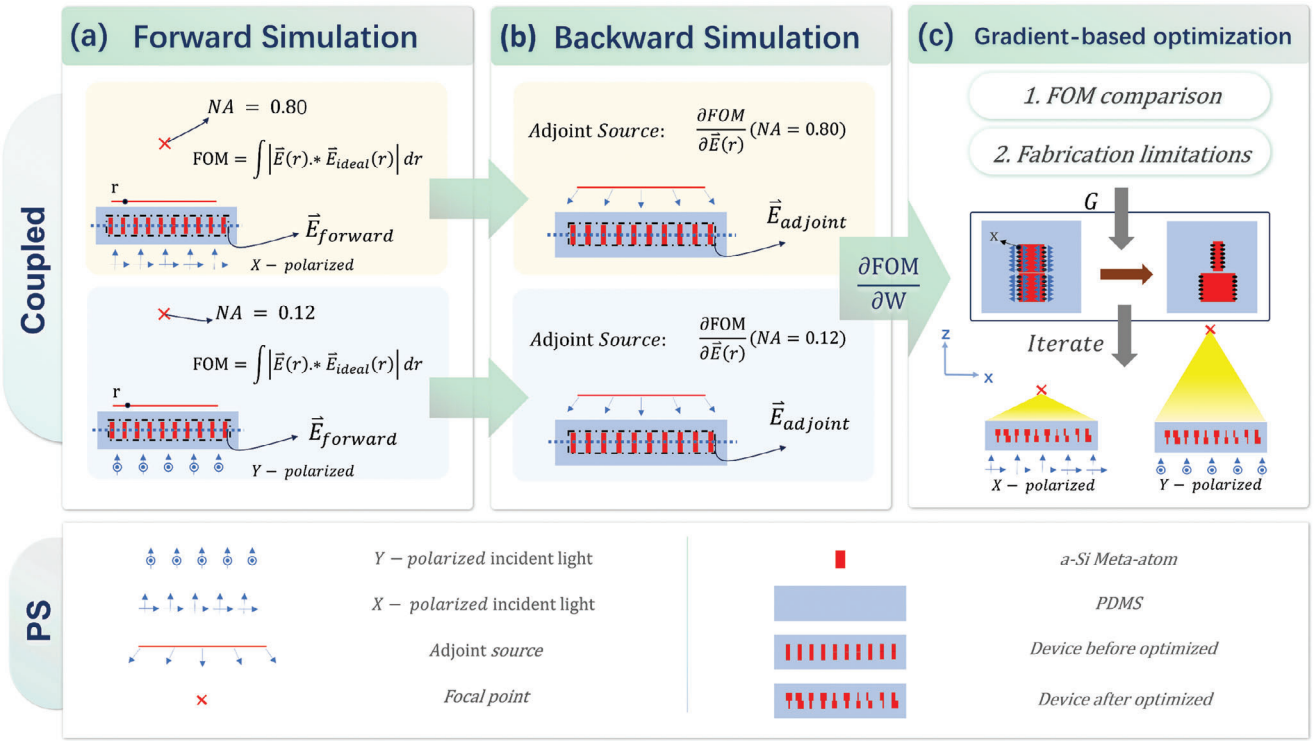

Figure 2. Design framework for coupled multilayer metasurface devices. a) In the forward simulation, X- and Y-polarized incident light are used as input sources to compute the *FOM* and the corresponding $E_{forward}$ separately. b) In the backward simulation, the gradients of different FOMs, $\frac{\partial FOM}{\partial \vec{E}(r)}$, are used as adjoint sources to compute the respective $E_{adjoint}$. c) The final gradient *G*, determined by the *FOM* and fabrication constraints, guides the optimization of structural parameters from *W* to *W′* through iterations to achieve the desired optical functionality.

based on the gradient descent method, the total gradient *G* is then used to update the meta-atom width from *W* to *W′*, as shown in Equation (5). Iterative calculations continue until the *FOM* meets our requirements. Additionally, to prevent excessive changes during iterations that could exceed manufacturing constraints, such as the period *P* and minimum feature size W_{strict}, we impose restrictions on the optimized width *W′* at the end of each iteration, as shown in Equation (6).

$$W' = W - G \tag{5}$$

$$W' < period\ P,\ W' > W_{strict} \tag{6}$$

To ensure the feasibility of the design, crucial parameters were referenced from our previous research.[7c] A refractive index of 3.2 for a-Si and 1.41 for PDMS was used at 940 nm. The PDMS layer is 200 μm thick, while the initial structure has a *W* of 200 nm, a *P* of 500 nm, a *h* of 740 nm, and W_{strict} set to 50 nm. The size of the device is ≈85λ. As a demonstration, the metalens's NA is set to 0.80 under X-polarized incident light and 0.12 under Y-polarized incident light.

Adopting the above method, we calculated the metasurface structure *W* of the upper and lower layers. **Figure 3** shows the X-Z plane and focal plane optical intensity distributions of the multilayer metalens under X-polarized and Y-polarized incident light, respectively, as calculated by the Finite Difference Time Domain (FDTD) method. Figure 3b,d show that under X-polarized light, the calculated focal length of 29.08 μm with an NA of 0.808 nearly matches the theoretical NA of 0.80. For Y-polarized light, the calculated focal length of 334.01 μm with an NA of 0.118 nearly matches the theoretical NA of 0.12.

NA is a key lens parameter directly linked to the focal spot's transverse and longitudinal resolution. Transverse resolution[7e,18] is defined as $\lambda/(2*NA)$, and longitudinal resolution[19] as $\lambda/(1-\sqrt{1-NA^2})$. An increased NA enhances both transverse and longitudinal resolutions, tailored to meet the specific requirements of diverse scenarios. In our design, as the polarization state of the incident light shifts from X to Y, the transverse resolution of the focal spot changes from 0.58 to 3.98 μm, achieving a modulation of 3.40 μm. Similarly, the longitudinal resolution varies from 2.28 to 136.23 μm, resulting in a modulation of 133.95 μm.

Efficiency is another crucial parameter of the metalens, including transmittance and focusing efficiency. We defined transmittance[20] as the ratio of transmitted power to incident power, resulting in 0.73 for X-polarized light and 0.70 for Y-polarized light. The focusing efficiency[20] is defined as the ratio of the power enclosed within an area with a radius three times the size of the FWHM spot, as shown in Figure 3c,e, to the incident power, resulting in 0.52 for X-polarized light and 0.60 for Y-polarized light.

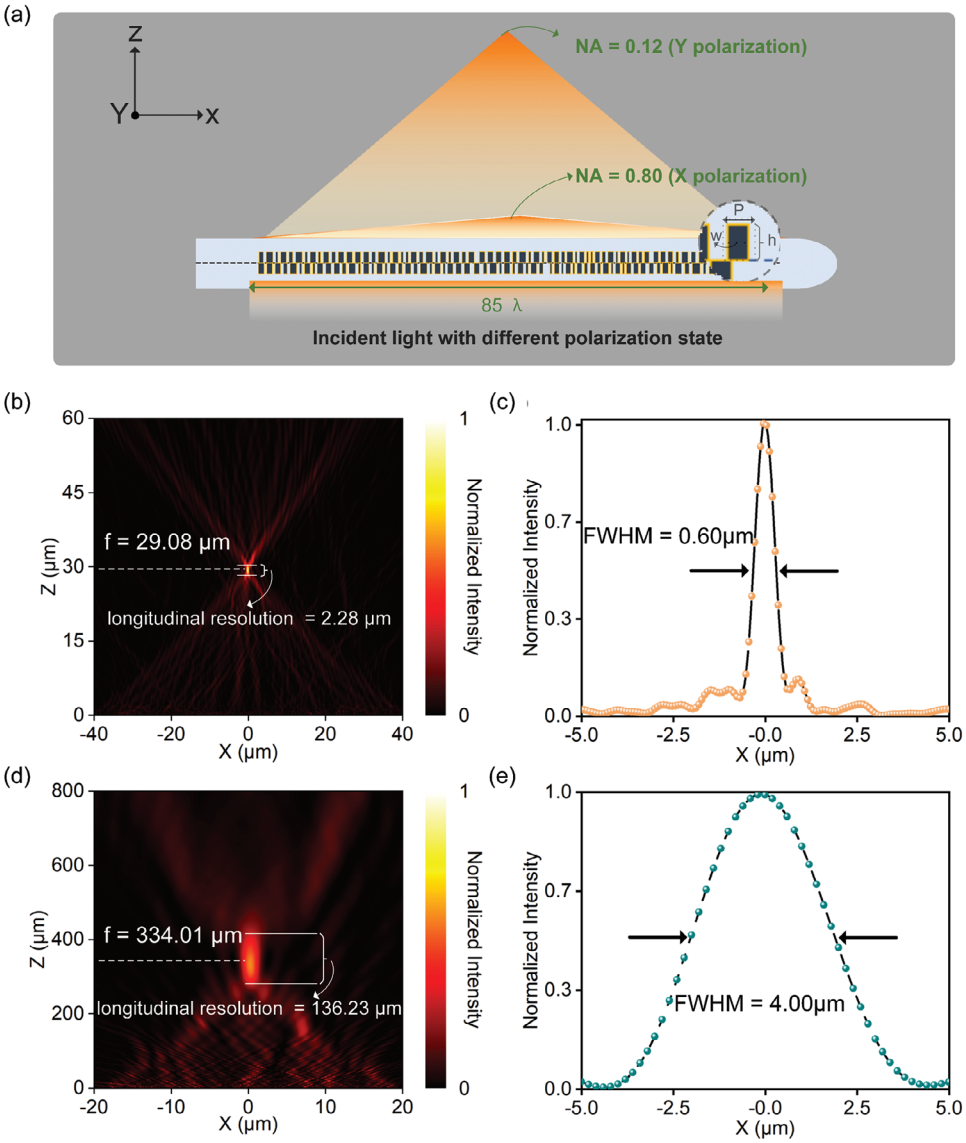

Figure 3. Schematic diagram and simulated optical performance of the multilayer zoom metalens. a) Schematic diagram of the multilayer zoom metalens on a foldable substrate. b) Simulated optical intensity distribution in the X-Z plane of the zoom metalens under X-polarized incident light. c) Simulated optical intensity profile at the focal plane of the zoom metalens under X-polarized incident light along the X axis. d) Simulated optical intensity distribution in the X-Z plane of the zoom metalens under Y-polarized incident light. e) Simulated optical intensity profile at the focal plane of the zoom metalens under Y-polarized incident light along the X-axis.

2.2. Assemblable Refractive-Meta Hybrid System Based on the Decoupled Multilayer Structure

In contrast to the coupled multilayer metasurface described in Section 2.1, the flexible substrate depicted in Figure 1b folds outward, resulting in a decoupled multilayer metasurface with a spacing significantly larger than a wavelength. In this configuration, traditional design methods[21] based on independent meta-atom remain effective due to the lack of layer-to-layer coupling.[7h,8a–c,g,h,j] Moreover, geometric optics mainly govern inter-layer propagation, making combining optical ray tracing and FDTD a helpful design approach. This structure also has better robustness to the incident angle, further reducing the impact of oblique incidence on the transmittance and phase of meta-atoms on curved substrates, thereby reducing the difficulty of operation on curved surfaces. Our optical design framework is illustrated in **Figure 4**. We first utilized scalar simulation in optical ray tracing to design the phase distribution of metalenses. Next, we used vector simulations in FDTD to determine the relationship among the meta-atom sizes, phases, and transmittances. Finally, we filled the metalenses with specific meta-atoms according to the phase distribution while ensuring high transmittance.

Inspired by commercial lenses that switch functions by combining a main lens with different sub-lenses. This section proposes a refractive-meta hybrid system on a decoupled multilayer metasurface structure. Our system allows the main and

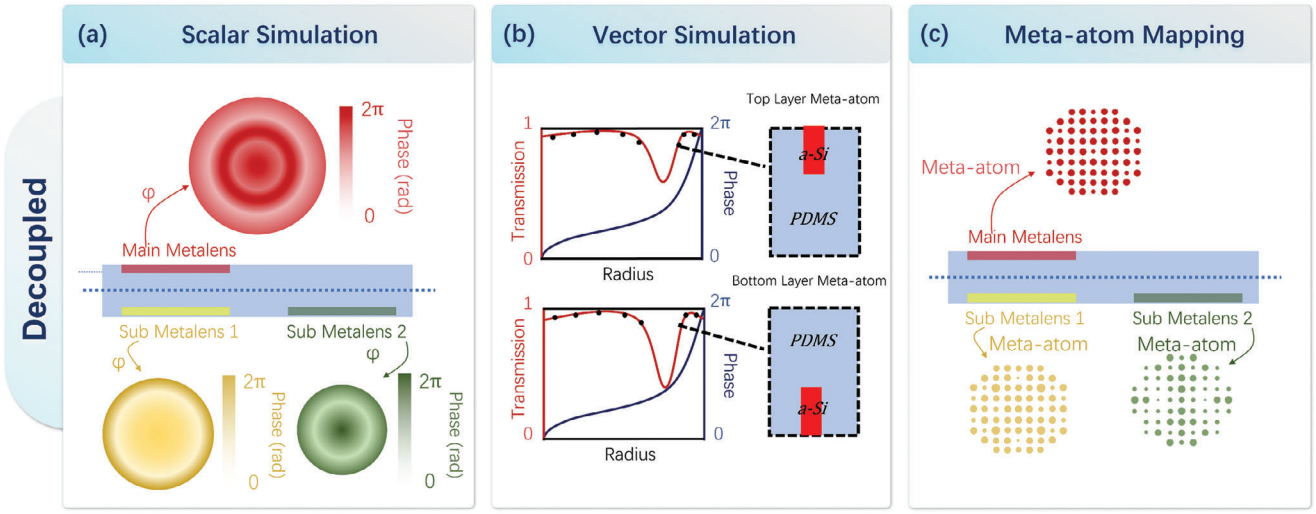

Figure 4. Design framework for decoupled multilayer metasurface devices. a) Scalar simulation determines the phase distribution of the top and bottom metasurface devices. b) Vector simulation achieves 2π phase coverage while maintaining high transmittance for the top and bottom meta-atoms. c) The meta-atoms are filled according to the phase distribution to obtain the final device.

sub-metalenses to be placed on separate layers, as illustrated in **Figure** 5a. By adjusting the folding positions to assemble the main metalens with various sub-metalenses and conform to a plano-convex lens, we achieved switchable functionalities between near-diffraction-limited telephoto and 80° FOV wide-angle mode. This demonstrates the conformability of the multilayer metalens to curved surfaces and its reconfigurable functionalities.

In the optical system, the aperture, with a radius of 0.325 mm, is positioned at the front focal plane of the refractive-meta hybrid lens, 1.025 mm from the curved substrate. This arrangement ensures the chief rays exit parallel to the optical axis, forming a telecentric design that effectively corrects off-axis aberrations.[22] The phase distributions for the telephoto and wide-angle modes are designed using an even-order polynomial, as described in Equation (7).[23]

$$\varphi(r) = \sum_{i=1}^{n} A_i \left(\frac{r}{R}\right)^{2i} \tag{7}$$

Where r is the radius to the center of the lens, R is the normalized radius, A_i is the coefficient of polynomial expansions, and n is the number of polynomial expansions. Typically, $n = 5$ is sufficient to meet design requirements.[23b]

In telephoto mode, with the main metalens aligned with sub-metalens 1, forming a multilayer metasurface centered on the plano-convex lens, resulting in a refractive-meta hybrid lens. The refractive-meta hybrid system has an effective focal length of 5.00 mm, corresponding to an F-number of 7.53. The coefficients for the metalens design are listed in Figure 5b.

The Modulation Transfer Function (MTF)[23a] is a key metric for lens resolution, measuring performance in two orientations: tangential and sagittal, to evaluate imaging quality and optical aberrations. Figure 5d illustrates the MTF of the metalens under 940 nm illumination for various FOV. Within a 0°–5° FOV, the MTF curve closely matches the diffraction limit in both tangential and sagittal directions, indicating high-precision imaging performance. Relative illuminance[23a] is a crucial metric for evaluating image quality, particularly for imaging lenses, as it reflects the uniformity of illumination across the image plane. It is defined as the illuminance ratio at different points on the image plane to that at the center point. Simulated results shown in Figure 5f demonstrate that within this FOV, the relative illuminance consistently remains above 0.98, indicating that the telephoto mode of our refractive-meta hybrid lens provides excellent imaging uniformity. Distortion[23a] is another important parameter in optical systems, reflecting the degree of geometric deformation in the image after light passes through the optical system. It is typically expressed as the percentage deviation of image point coordinates. In the design of telephoto lenses, pincushion distortion is more likely to occur, while barrel distortion is common in the design of wide-angle lenses.[24] In our telephoto mode lens design, pincushion distortion was observed as well. As the FOV expands, the distortion gradually increases positively. However, at a 5° FOV, distortion remains below 2%, making it nearly imperceptible to the human eye. We further simulated imaging by convolving the lens's point spread function (PSF) with a 30° field height object, as shown in Figure 5g. The imaging results at a 3° FOV in Figure 5h demonstrate the narrow FOV, near-diffraction-limited, and excellent relative illuminance of the telephoto mode.

In wide-angle mode, with the main metalens aligned with sub-metalens 2, the optical system is configured as shown in Figure 5c. The refractive-meta hybrid system's effective focal length is reduced to 1.64 mm (with an F-number of 2.47), achieving a 40° FOV. Figure 5e presents the MTF curves under 940 nm illumination. Within the 0°–40° FOV, the MTF curves approach the diffraction limit at spatial frequencies up to 20 lp mm^{-1}, after which the differences become increasingly noticeable. The tangential MTF curve at a 40° FOV shows the greatest deviation from the diffraction limit; however, it remains above 0.55 at 80 lp mm^{-1}, indicating great wide-angle imaging performance. The relative illumination of the refractive-meta hybrid lens consistently exceeds 0.78 within a 0°–40° FOV, as shown in Figure 5f,

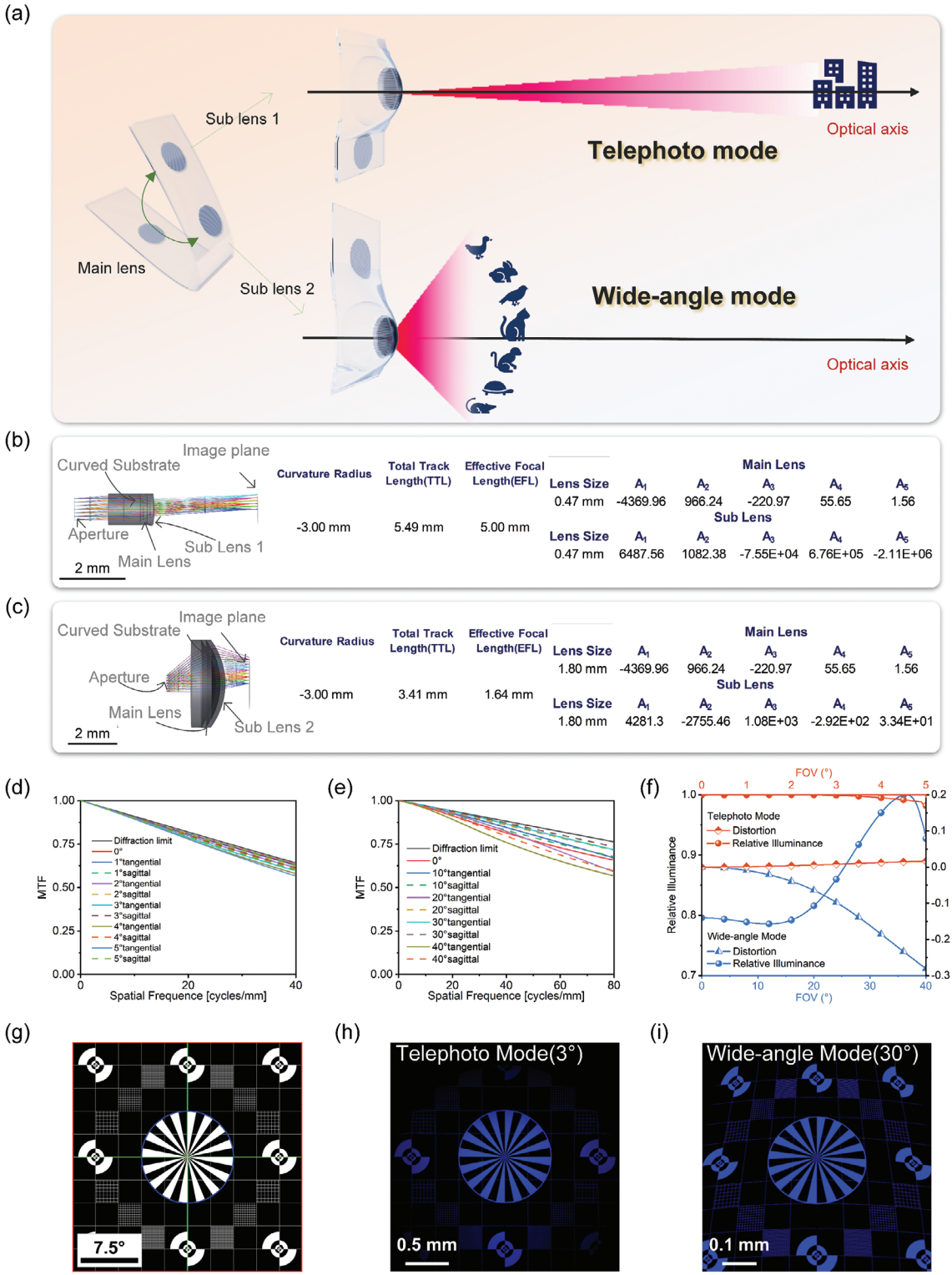

Figure 5. Schematic diagram and simulation results of the optical performance of the refractive-meta hybrid systems. a) Schematical diagram of the refractive-meta hybrid lens with functionality switching between telephoto and wide-angle modes. b) Designed layout and key parameters of the telephoto mode refractive-meta hybrid lens. c) Designed layout and key parameters of the wide-angle mode refractive-meta hybrid lens. d) Nominal MTF as a function of spatial frequency for the telephoto mode refractive-meta hybrid system. e) Nominal MTF as a function of spatial frequency for the wide-angle mode refractive-meta hybrid system. f) Relative illuminance and distortion as functions of FOV for the telephoto and wide-angle modes of the refractive-meta hybrid systems. g) Imaging object with a field height of 30°. h) Imaging result of the telephoto mode refractive-meta hybrid system at a 3° FOV. i) Imaging result of the wide-angle mode refractive-meta hybrid system at a 30° FOV.

demonstrating uniform imaging brightness. Wide-angle lenses typically exhibit distortion; however, this distortion does not affect the overall imaging resolution and can be further corrected by algorithms.[25] Generally, viewers find distortion within 10% acceptable.[23a] In the wide-angle mode lens we designed, the distortion within this FOV range exhibits negative ("barrel") distortion, reaching −27% at a 40° FOV and −5% at a 20° FOV, as shown in Figure 5f. Imaging simulations at a 30° FOV, illustrated in Figure 5i, highlight the wide FOV, high resolution, and consistent relative illumination of the wide-angle mode.

After performing scalar simulations in optical ray tracing, we determined the phase distribution generated by the coefficients of the main metalens and two sub-metalenses. Unlike traditional lenses, the phase distribution of a metalens consists of discrete meta-atoms. In contrast to the coupled multilayer metasurfaces discussed in Section 2.1, the structures from different layers here are decoupled, allowing the meta-atoms to operate independently based on various principles such as propagation phase,[7c,d,26] resonance phase,[5d,27] geometric phase,[3a,5c,28] or other types. Leveraging our experience in creating propagation phase-type metasurfaces,[7c] we employed cylindrical metasurfaces, as illustrated in **Figure 6**a. The top and bottom a-Si pillar meta-atoms of the multilayer metasurfaces are positioned in a mirrored PDMS environment. The refractive indices for the materials are 3.2 for a-Si and 1.41 for PDMS, respectively. FDTD vector simulations confirmed that these meta-atoms, with a radius ranging from 0.05 to 0.14 μm, a height of 0.74 μm, and a period of 0.45 μm, can achieve 2π phase coverage while maintaining high transmission efficiency above 0.9 under normal incidence, as shown in Figure 6b.

When a metasurface conforms to a non-planar object, the incident angle varies across the surface. Therefore, low sensitivity to the incident angle is crucial for conformal metasurfaces. We simulated the phase and transmittance performance of two layers of meta-atoms with radius ranging from 0.05 to 0.14 μm at incident angles from 0° to 30°, as shown in the left part of Figure 6c,d. The results show minimal phase variation with changing incident angles, and the rate of phase change is nearly identical across all meta-atoms. This characteristic is essential for the system shown in Figure 5b,c, ensuring consistency in the normalized phase distribution across different FOVs. Additionally, the transmittance remains nearly unaffected as the incident angle changes, demonstrating consistent relative illumination across various FOVs. To further understand the phase stability while maintaining high transmittance, we analyzed the electromagnetic field distribution in the X-Y and X-Z planes of meta-atoms with a radius of 0.135 μm from the bottom and top layers at incident angles of 0° and 30°, as shown in Figure 6c,d, respectively. In Figure 6c (i),d (i), under normal incidence, light is concentrated within the meta-atoms of the two layers, showing characteristics of weakly coupled, low-quality factor resonators.[12a] Even at an incident angle of 30°, as shown in Figure 6c (ii),d (ii), the energy remains confined within the meta-atoms, with minimal changes in the electromagnetic field. This is due to the significant difference in refractive indices between a-Si and the surrounding medium,[20] effectively localizing energy within the a-Si. After selecting the appropriate meta-atoms, we populated the final main and sub-lens layouts according to the phase distribution shown in Figure 6e, which was obtained from scalar simulation.

3. Discussion

In the fabrication of multilayer devices, the alignment precision between layers is crucial to their performance. Compared to decoupled multilayer metasurfaces, coupled multilayer metasurfaces rely on specific structural distributions, which impose even stricter requirements on process precision. To reduce the impact of alignment errors, the optical performance under various process deviation scenarios can be optimized in the design phase.[16] For the fabrication of decoupled multilayer metasurfaces, the alignment photomask marker method is widely used.[7h,8h,29] Here, the combination of the alignment photomask marker method with the flexible metasurface fabrication process we developed[7c] provides a reference for the fabrication of flexible decoupled multilayer metasurfaces, as detailed in Figure S2 (Supporting Information).

Furthermore, to evaluate the impact of alignment errors of varying degrees on the performance of decoupled multilayer devices, we calculated and analyzed the effects of both the overall alignment errors between the main optical axes of the two metasurfaces and the refractive lens (ranging from 0 to 4 μm), as well as the local alignment errors between the main optical axes of the two metasurfaces (ranging from 2 to 4 μm) on the MTF, considering both wide-angle and telephoto modes. The results in Figure S3 (Supporting Information) show that performance in telephoto mode is minimally affected by alignment errors, remaining close to the diffraction limit. In wide-angle mode, the outer field is more significantly impacted by alignment errors, particularly local alignment errors. However, within a range of 0–3 μm for overall alignment errors and 0–2 μm for local alignment errors, the MTF across all FOVs remains above 0.45 in the 0–80 lp mm^{-1} range. This demonstrates the robustness of multilayer devices to alignment errors, highlighting their practical feasibility in real-world applications.

For performance characterization, the optical field and efficiency tests of coupled multilayer devices can be conducted using the testing setup and methods we previously developed.[7c] For decoupled multilayer devices in terms of MTF, relative illumination, distortion, and other parameters at different FOVs, the reported testing methods for wide-angle metalens could be applied.[23a,30]

In practical applications, to enable precise fold control, flexible metasurfaces can be integrated with miniaturized precision mechanical modules, using various actuation methods such as electroactive, thermal, or magnetic actuation to adjust the device's folding position and direction.

4. Conclusion

In this work, we present an innovative multilayer metasurface platform that capitalizes on the foldability and conformality inherent in flexible metasurfaces. This novel approach not only facilitates the design of both coupled and decoupled multilayer metasurface structures but also extends its functionality and reconfigurability to curved substrates, surpassing the capabilities of existing methods.

To illustrate the capabilities of this platform for coupled multilayer metasurfaces, we utilized an adjoint-based topology boundary optimization algorithm to design a 1D multilayer zoom

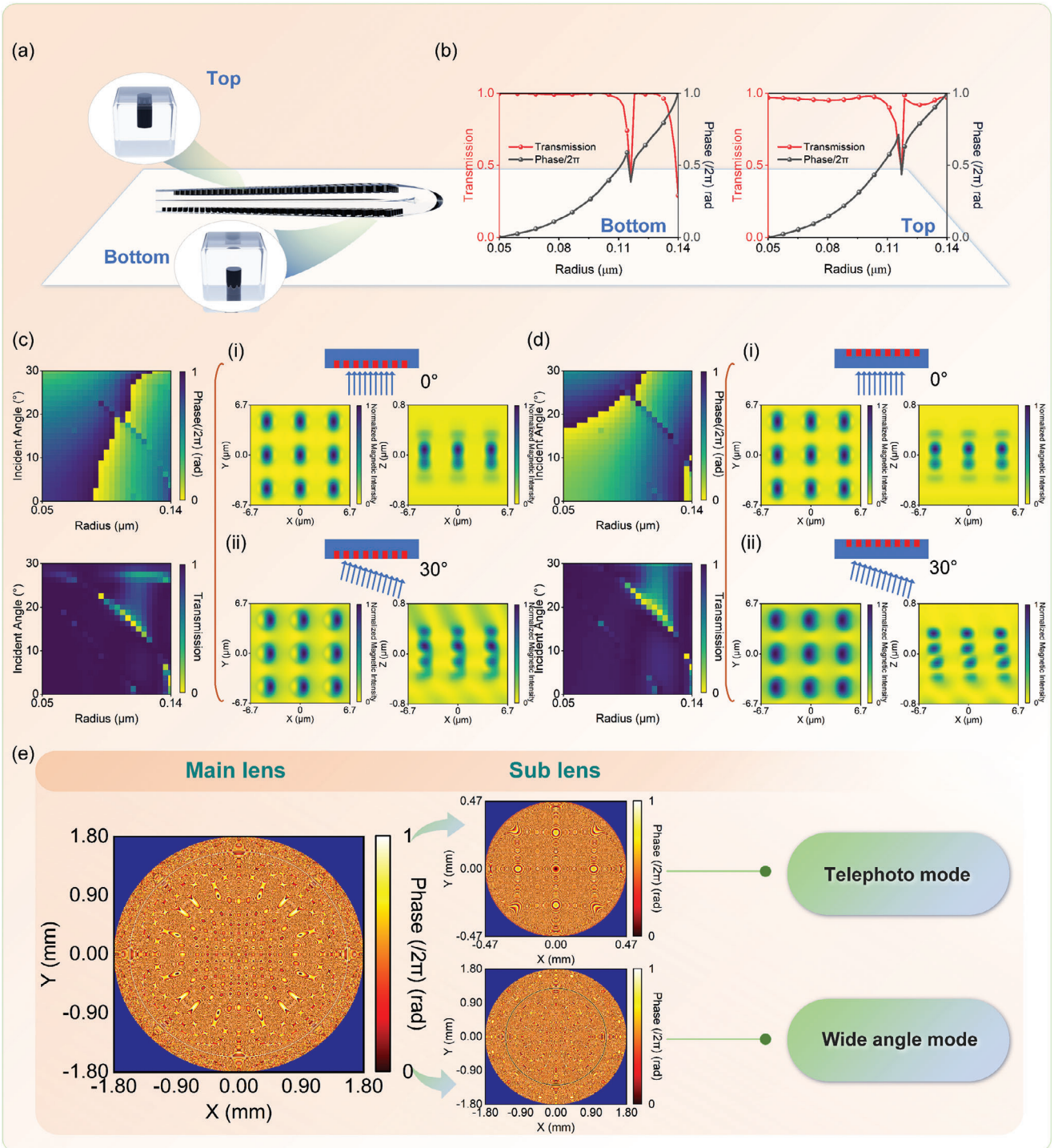

Figure 6. Schematic diagram of the top and bottom meta-atoms of a decoupled multilayer metasurface structure, along with the optical performance of these meta-atoms at varying incident angles and the final phase distribution of the main and sub-metalenses. a) Schematic of the top and bottom meta-atoms based on the decoupled multilayer metasurface structure. b) Transmission and phase as functions of radius for top and bottom meta-atoms under normal incidence. c) Transmission and phase of the bottom meta-atoms as functions of varying incident angle, along with the electromagnetic field distributions in the X-Y and X-Z planes at (i) 0° and (ii) 30° incidence. d) Transmission and phase of the top meta-atoms as functions of varying incident angle, along with the electromagnetic field distributions in the X-Y and X-Z planes at (i) 0° and (ii) 30° incidence. e) Overall phase distribution of main metalens and sub-metalenses.

metalens. Its NA can be significantly modulated by adjusting the polarization state of the incident light from X to Y, varying from 0.80 to 0.12. This results in a lateral resolution variation of 3.40 μm and an axial resolution variation of 133.95 μm. Additionally, we designed multilayer metalens for curved surfaces as a refractive-meta hybrid system for the decoupled multilayer metasurfaces. This system can switch between a near-diffraction-limited telephoto mode and an 80° FOV wide-angle mode. Building on the simulated demonstration of these two types of devices, we are confident that this multilayer metasurface platform, leveraging the folding and conformal capabilities of flexible substrates, will provide innovative solutions for the development of multilayer metasurface devices. Moreover, this platform is poised to accelerate the evolution of multifunctional and compact optoelectronic devices such as augmented reality displays and wearable medical devices.

Supporting Information

Supporting Information is available from the Wiley Online Library or from the author.

Acknowledgements

This work was primarily supported by the National Natural Science Foundation of China (62175202, 92150302); "Pioneer" and "Leading Goose" R&D Program of Zhejiang Province (2024SDXHDX0005), Zhejiang Provincial Natural Science Foundation of China (LD22F040002); Key Project of Westlake Institute for Optoelectronics (2023GD003/110500Y0022303); Research Center for Industries of the Future (RCIF) at Westlake University (Grant No. 210230006022302/002); Special Support Plan for Photoelectric Chips Research at Westlake University (10300000H062401/001); Start-up fund of Westlake University.

Conflict of Interest

The authors declare no conflict of interest.

Author Contributions

All the authors have accepted responsibility for the entire content of this submitted manuscript and approved the submission.

Data Availability Statement

The data that support the findings of this study are available from the corresponding author upon reasonable request.

Keywords

flexible metasurface, inverse design, multilayer metasurface, reconfigurable metasurface

Received: December 16, 2024
Published online: February 6, 2025

[1] M. D. Aiello, A. S. Backer, A. J. Sapon, J. Smits, J. D. Perreault, P. Llull, V. M. Acosta, *ACS Photonics* **2019**, *6*, 2432.
[2] A. Tricoli, N. Nasiri, S. De, *Adv. Funct. Mater.* **2017**, *27*, 1605271.
[3] a) N. Yu, P. Genevet, M. A. Kats, F. Aieta, J.-P. Tetienne, F. Capasso, Z. Gaburro, *Science* **2011**, *334*, 333; b) C. Jung, E. Lee, J. Rho, *Sci. Adv.* **2024**, *10*, eado8964.
[4] C. Meng, P. C. Thrane, F. Ding, J. Gjessing, M. Thomaschewski, C. Wu, C. Dirdal, S. I. Bozhevolnyi, *Sci. Adv.* **2021**, *7*, eabg5639.
[5] a) Y. Ni, S. Chen, Y. Wang, Q. Tan, S. Xiao, Y. Yang, *Nano Lett.* **2020**, *20*, 6719; b) Z. Li, Q. Dai, M. Q. Mehmood, G. Hu, B. L. Yanchuk, J. Tao, C. Hao, I. Kim, H. Jeong, G. Zheng, *Light: Sci. Appl.* **2018**, *7*, 63; c) G. Kim, Y. Kim, J. Yun, S.-W. Moon, S. Kim, J. Kim, J. Park, T. Badloe, I. Kim, J. Rho, *Nat. Commun.* **2022**, *13*, 5920; d) S. Sun, Q. He, S. Xiao, Q. Xu, X. Li, L. Zhou, *Nat. Mater.* **2012**, *11*, 426; e) E. Choi, G. Kim, J. Yun, Y. Jeon, J. Rho, S.-H. Baek, *Nat. Photonics* **2024**, *18*, 848.
[6] a) X. Zhang, S. Yang, W. Yue, Q. Xu, C. Tian, X. Zhang, E. Plum, S. Zhang, J. Han, W. Zhang, *Optica* **2019**, *6*, 1190; b) B. Xiong, Y. Liu, Y. Xu, L. Deng, C.-W. Chen, J.-N. Wang, R. Peng, Y. Lai, Y. Liu, M. Wang, *Science* **2023**, *379*, 294; c) X. Ding, Z. Wang, G. Hu, J. Liu, K. Zhang, H. Li, B. Ratni, S. N. Burokur, Q. Wu, J. Tan, *PhotoniX* **2020**, *1*, 1; d) S. So, J. Kim, T. Badloe, C. Lee, Y. Yang, H. Kang, J. Rho, *Adv. Mater.* **2023**, *35*, 2208520; e) H. Kang, H. Kim, K. Kim, J. Rho, *ACS Nano* **2024**, *18*, 21504; f) I. Kim, J. Jang, G. Kim, J. Lee, T. Badloe, J. Mun, J. Rho, *Nat. Commun.* **2021**, *12*, 3614.
[7] a) M. Y. Shalaginov, S. An, Y. Zhang, F. Yang, P. Su, V. Liberman, J. B. Chou, C. M. Roberts, M. Kang, C. Rios, *Nat. Commun.* **2021**, *12*, 1225; b) R. Paniagua-Dominguez, Y. F. Yu, E. Khaidarov, S. Choi, V. Leong, R. M. Bakker, X. Liang, Y. H. Fu, V. Valuckas, L. A. Krivitsky, *Nano Lett.* **2018**, *18*, 2124; c) Y. Shi, H. Dai, R. Tang, Z. Chen, Y. Si, H. Ma, M. Wei, Y. Luo, X. Li, Q. Zhao, *Nanophotonics* **2024**, *13*, 1339; d) H. Pahlevaninezhad, M. Khorasaninejad, Y.-W. Huang, Z. Shi, L. P. Hariri, D. C. Adams, V. Ding, A. Zhu, C.-W. Qiu, F. Capasso, *Nat. Photonics* **2018**, *12*, 540; e) M. Ossiander, M. L. Meretska, H. K. Hampel, S. W. D. Lim, N. Knefz, T. Jauk, F. Capasso, M. Schultze, *Science* **2023**, *380*, 59; f) X. Zou, G. Zheng, Q. Yuan, W. Zang, R. Chen, T. Li, L. Li, S. Wang, Z. Wang, S. Zhu, *PhotoniX* **2020**, *1*, 1; g) Z. Li, P. Lin, Y.-W. Huang, J.-S. Park, W. T. Chen, Z. Shi, C.-W. Qiu, J.-X. Cheng, F. Capasso, *Sci. Adv.* **2021**, *7*, eabe4458; h) E. Arbabi, A. Arbabi, S. M. Kamali, Y. Horie, M. Faraji-Dana, A. Faraon, *Nat. Commun.* **2018**, *9*, 812; i) J. Chen, X. Ye, S. Gao, Y. Chen, Y. Zhao, C. Huang, K. Qiu, S. Zhu, T. Li, *Optica* **2022**, *9*, 431; j) J. Kim, J. Seong, W. Kim, G.-Y. Lee, S. Kim, H. Kim, S.-W. Moon, D. K. Oh, Y. Yang, J. Park, *Nat. Mater.* **2023**, *22*, 474.
[8] a) O. Avayu, E. Almeida, Y. Prior, T. Ellenbogen, *Nat. Commun.* **2017**, *8*, 14992; b) P. Georgi, Q. Wei, B. Sain, C. Schlickriede, Y. Wang, L. Huang, T. Zentgraf, *Sci. Adv.* **2021**, *7*, eabf9718; c) H. Kwon, E. Arbabi, S. M. Kamali, M. Faraji-Dana, A. Faraon, *Nat. Photonics* **2020**, *14*, 109; d) Z. Lin, B. Groever, F. Capasso, A. W. Rodriguez, M. Lončar, *Phys. Rev. Appl.* **2018**, *9*, 044030; e) P. Camayd-Muñoz, C. Ballew, G. Roberts, A. Faraon, *Optica* **2020**, *7*, 280; f) H. Chung, O. D. Miller, *Opt. Express* **2020**, *28*, 6945; g) L. Zhang, L. Zhang, R. Xie, Y. Ni, X. Wu, Y. Yang, F. Xing, X. Zhao, Z. You, *Adv. Sci.* **2023**, *10*, 2300542; h) Z. Han, S. Colburn, A. Majumdar, K. F. Böhringer, *Microsyst. Nanoeng.* **2020**, *6*, 79; i) Z. Lin, V. Liu, R. Pestourie, S. G. Johnson, *Opt. Express* **2019**, *27*, 15765; j) S. Colburn, A. Zhan, A. Majumdar, *Optica* **2018**, *5*, 825.
[9] A. I. Kuznetsov, M. L. Brongersma, J. Yao, M. K. Chen, U. Levy, D. P. Tsai, N. I. Zheludev, A. Faraon, A. Arbabi, N. Yu, *ACS Photonics* **2024**, *11*, 816.
[10] Y. Wei, Y. Wang, X. Feng, S. Xiao, Z. Wang, T. Hu, M. Hu, J. Song, M. Wegener, M. Zhao, *Adv. Opt. Mater.* **2020**, *8*, 2000142.
[11] B. Groever, W. T. Chen, F. Capasso, *Nano Lett.* **2017**, *17*, 4902.
[12] a) S. M. Kamali, A. Arbabi, E. Arbabi, Y. Horie, A. Faraon, *Nat. Commun.* **2016**, *7*, 11618; b) J. Kim, H. Kim, H. Kang, W. Kim, Y. Chen, J.

Choi, H. Lee, J. Rho, *Nat. Food* **2024**, *5*, 293; c) J. Ko, G. Kim, I. Kim, S. H. Hwang, S. Jeon, J. Ahn, Y. Jeong, J. H. Ha, H. Heo, J. H. Jeong, *Adv. Sci.* **2024**, *11*, 2407045.
[13] J. Xiao, R. I. Hunter, D. A. Robertson, G. M. Smith, S. Horsley, S. A. Schulz, A. D. Falco, *Adv. Mater. Technol.* **2023**, *8*, 2202006.
[14] T. Badloe, I. Kim, Y. Kim, J. Kim, J. Rho, *Adv. Sci.* **2021**, *8*, 2102646.
[15] O. D. Miller, in *Photonic design: From fundamental solar cell physics to computational inverse design*, University of California, Berkeley, CA, USA, **2012**.
[16] D. Sell, J. Yang, S. Doshay, R. Yang, J. A. Fan, *Nano Lett.* **2017**, *17*, 3752.
[17] Z. Li, R. Pestourie, J.-S. Park, Y.-W. Huang, S. G. Johnson, F. Capasso, *Nat. Commun.* **2022**, *13*, 1.
[18] W. T. Chen, A. Y. Zhu, M. Khorasaninejad, Z. Shi, V. Sanjeev, F. Capasso, *Nano Lett.* **2017**, *17*, 3188.
[19] T.-C. Poon, in *Digital holography and three-dimensional display: Principles and Applications*, Springer Science & Business Media, Berlin, Germany **2006**.
[20] A. Arbabi, Y. Horie, A. J. Ball, M. Bagheri, A. Faraon, *Nat. Commun.* **2015**, *6*, 7069.
[21] H. Cai, S. Srinivasan, D. A. Czaplewski, A. B. Martinson, D. J. Gosztola, L. Stan, T. Loeffler, S. K. Sankaranarayanan, D. López, *npj Comput. Mater.* **2020**, *6*, 116.
[22] D. A. Buralli, G. M. Morris, *Appl. Opt.* **1989**, *28*, 3950.
[23] a) J. Engelberg, C. Zhou, N. Mazurski, J. Bar-David, A. Kristensen, U. Levy, *Nanophotonics* **2020**, *9*, 361; b) S. Luo, F. Zhang, X. Lu, T. Xie, M. Pu, Y. Guo, Y. Wang, X. Luo, *J. Phys. D: Appl. Phys.* **2022**, *55*, 235106.
[24] L. Stroebel, in *View Camera Technique*, Routledge, New York **1999**.
[25] S. Van der Jeught, J. A. Buytaert, J. J. Dirckx, *Opt. Eng.* **2012**, *51*, 027002.
[26] S. M. Kamali, E. Arbabi, A. Arbabi, Y. Horie, A. Faraon, *Laser Photonics Rev.* **2016**, *10*, 1002.
[27] S. Sun, K.-Y. Yang, C.-M. Wang, T.-K. Juan, W. T. Chen, C. Y. Liao, Q. He, S. Xiao, W.-T. Kung, G.-Y. Guo, *Nano Lett.* **2012**, *12*, 6223.
[28] Q. Fan, W. Xu, X. Hu, W. Zhu, T. Yue, C. Zhang, F. Yan, L. Chen, H. J. Lezec, Y. Lu, *Nat. Commun.* **2022**, *13*, 2130.
[29] a) Y. Zhou, H. Zheng, I. I. Kravchenko, J. Valentine, *Nat. Photonics* **2020**, *14*, 316; b) Y. Zhou, I. I. Kravchenko, H. Wang, J. R. Nolen, G. Gu, J. Valentine, *Nano Lett.* **2018**, *18*, 7529.
[30] Q. Chen, J. Zhou, S. Pian, J. Xu, X. Li, B. Li, C. Lu, Z. Wang, Q. Jiang, S. Qin, *ACS Photonics* **2024**, *11*, 3794.